Infection, Genetics and Evolution 69 (2019) 176–189

Contents lists available at ScienceDirect

Infection, Genetics and Evolution

journal homepage: www.elsevier.com/locate/meegid

Research paper

Zika virus induces abnormal cranial osteogenesis by negatively affecting cranial neural crest development

Yuqi Yan[a,c,1], Xiao-tan Zhang[a,1], Guang Wang[a], Xin Cheng[a], Yu Yan[a], Ying-jie Fu[a,c], Xuesong Yang[a,b,*], Zhenyou Jiang[a,c,**]

[a] Medical College, Jinan University, Guangzhou 510632, China
[b] Key Laboratory for Regenerative Medicine of the Ministry of Education, Medical College, Jinan University, Guangzhou 510632, China
[c] Institute of Medical Microbiology, Jinan University, Guangzhou, 510632, Guangdong, China

ARTICLE INFO

Keywords:
ZIKV
Microcephaly
Osteogenesis
Cranial neural crest cells
EMT
Apoptosis

ABSTRACT

Zika virus (ZIKV) infection during gestation is deemed to be coupled to birth defects through direct impairment of the nervous system during neurogenesis. However, in this study, our data showed that ZIKV infection dramatically suppressed cranial osteogenesis, shown by Safranin O/Fast Green and alizarin red staining, in chick embryos, which provides another possibility that craniofacial bone malformation caused by ZIKV may be a major cause of ZIKV-mediated birth defects. By immunofluorescent staining and electron microcopy, we confirmed ZIKV infection in chick embryo neural tubes and sites of neural crest. Next, *in vivo* (chick embryos) and *in vitro* [primary culture of neural crest cells (NCC)] ZIKV and HNK-1 double immunofluorescent staining demonstrated that ZIKV infection inhibited the production of migratory NCC. The reduction of both AP-2α- and Pax7-positive NCC in HH10 chick embryos infected by ZIKV confirmed that abnormal development of cranial NCC also occurred in the migratory process. Whole mount *in situ* hybridization demonstrated that cadherin 6B expression was elevated and Slug, FoxD3, and BMP4/Msx1 expressions decreased in ZIKV-infected HH10 chick embryos, implying that epithelial–mesenchymal transition (EMT) of neural crest production was blocked by ZIKV infection. Moreover, *in vivo* and *in vitro* pHIS3 and Pax7 double immunofluorescent staining showed that NCC proliferation was repressed by ZIKV infection. C-caspase-3 and AP-2α double immunofluorescent staining in HH10 chick embryos and western blotting showed that NCC apoptosis increased following ZIKV infection. Finally, electron microscopy showed multiple autophagosomes in ZIKV-infected embryos, and western blot and LC3B immunofluorescent staining demonstrated that autophagy-related genes were activated by ZIKV infection. Taken together, our data first showed that ZIKV infection during embryogenesis could interfere with cranial neural crest development, which in turn causes aberrant cranial osteogenesis. Our results provided new insights into brain malformations induced by ZIKV infection.

1. Introduction

Zika virus (ZIKV) is a mosquito-borne flavivirus that caused great epidemics in the Latin America and Pacific Ocean region (Tappe et al., 2016). Little attention was paid to ZIKV infection-induced disorders until ten years ago when the outbreak was first reported (Rodriguez-Morales, 2015). This is, in part, because it was recognized as a mild disease and, thus, researchers ignored the importance of studying this virus (Maharajan et al., 2016). ZIKV infection in humans is principally transmitted through the bites of *Aedes aegypti* mosquito (Fernandez-Garcia et al., 2009). However, it is noteworthy that ZIKV could also be transmitted through blood transfusion, perinatal infection, and sexual intercourse (Triunfol, 2016; Besnard et al., 2014). Therefore, pregnant women should avoid travelling in the endemic areas of ZIKV transmission because ZIKV infection is deemed to be directly coupled to the most conspicuous of the birth defects, microcephaly, as indicated by clinical and epidemiological studies (Maharajan et al., 2016; Rothan et al., 2018). Of late, ZIKV infection has become an international health concern and has been declared as a public health emergency by the World Health Organization.

ZIKV infection and ZIKV-induced neurological damages in neonates increase the risk of infectious diseases (Petersen et al., 2016).

* Corresponding author at: Medical College, Jinan University, Guangzhou 510632, China.
** Corresponding author at: Medical College, Jinan University, Guangzhou 510632, China
E-mail addresses: yang_xuesong@126.com, yangxuesong@jnu.edu.cn (X. Yang), tjzhy@jnu.edu.cn (Z. Jiang).
[1] These two authors contributed equally to the work.

https://doi.org/10.1016/j.meegid.2019.01.023
Received 8 October 2018; Received in revised form 17 January 2019; Accepted 18 January 2019
Available online 19 January 2019

Accumulating evidence has indicated the causality between ZIKV infection and birth defects, which accompanies rigorous fetal brain injury in case of vertically acquired ZIKV infection (Vesnaver et al., 2017; Mlakar et al., 2016a; Dick, 1952). For example, maternal ZIKV infection can be transmitted to the fetus because ZIKV is found in the amniotic fluid of the pregnant women and the fetus suffers from microcephaly (Calvet et al., 2016). Moreover, six ZIKV-infected children birthed by ZIKV-infected mothers had neonatal head circumferences below the 10th percentile in a few regions of Brazil (Cofre, 2016; Oliveira Melo et al., 2016). Taken together, the characteristics of ZIKV infection reflect on the strong tropism towards the developing brain and eye. Thus, ZIKV can cause neurodevelopmental dysfunction, including microcephaly (Tetro, 2016), which has been observed in intraperitoneally inoculated mice (Dick, 1952). However, there is another possibility that ZIKV infection-induced brain malformations may be primarily due to the dysplasia of craniofacial skeleton, and neurodevelopmental disorder is the secondary or passive reason. Therefore, we meticulously investigated the same in this study using early chick embryos infected by ZIKV.

The skull (cranium) consists of the neurocranium and viscerocranium, and it develops from the mesenchyme, which is derived from the neural crest and paraxial mesoderm. The neural crest cells (NCC) form the mesenchyme at the head region and migrate into the pharyngeal arches to form the bones and connective tissue of the face (craniofacial skeleton). The craniofacial skeleton of vertebrates primarily originates from cranial neural crest cells (CNC) (Bronner, 2015). NCC have the remarkable ability to migrate extensively within the developing embryo and differentiate like pluripotent cells into many tissue derivatives (Simoes-Costa and Bronner, 2015). Therefore, the neural crest is sometimes referred to as the fourth embryonic germ layer. Neural crest originates from the borders of the neural plate and undergoes the process of neural induction, delamination, epithelial–mesenchymal transition (EMT), migration, and differentiation into the terminal tissues (Hall, 2008). In the cranial region, the cranial neural crest contributes to all of the craniofacial skeleton, cerebral ganglions, enteric nervous system, and Schwann cells (Cordero et al., 2011; Schneider, 1999). Neural crest development is spatiotemporally regulated by a series of epigenetic genes (Simoes-Costa and Bronner, 2015), and dysplasia of the neural crest could result in neural tube defects, atrioventricular septal defect, patent ductus arteriosus, and Waardenburg syndrome (Tetro, 2016; Penchaszadeh et al., 1982; Blazquez et al., 2014).

NCCs are particularly extensively sensitive to external stress because they migrate, and the differentiated NCCs are vulnerable to detrimental factors during embryonic development. Scientists have revealed many congenital disorders that are due to the dysplasia of NCC during gestation. For example, hyperglycemia from diabetes impairs the differentiation ability of the cranial neural crest into the cranial bone (Rothan et al., 2018). In this study, we employed a chick embryo model (Datar and Bhonde, 2011; Scott-Drechsel et al., 2013) to investigate whether ZIKV infection-induced brain malformations is associated with abnormal cranial osteogenesis and to elucidate the underlying cellular and molecular mechanisms.

2. Results

2.1. ZIKV infection caused abnormal craniofacial osteogenesis in chick embryos

To study the effect of ZIKV infection on embryo development, we windowed 2-day incubated fertilized eggs, injected ZIKV into the cranial neural tubes, and further incubated the eggs until day 9 (Fig. 1A). The result showed that ZIKV infection caused death of few embryos, although the number was not high (Fig. 1B). The weight of 9-day embryo reduced dramatically compared to that of the control (Fig. 1C). We checked if the chick embryos were successfully infected by ZIKV and observed ZIKV RNA expression in chick embryos, with the distribution of virus RNA copy numbers being the highest to lowest in the brain, eyes, and trunk (Fig. 1D). ZIKV PFU in each gram of chick embryo tissue of the brain and eyes was almost similar, but was much lower in the trunk (Fig. 1E). In comparison to the 9-day chick embryo heads, we demonstrated that ZIKV infection significantly reduced the skull length, cranial height, and biparietal diameters (Fig. 1L), which was achieved through measuring external dimensions of the 9-day chick embryos (Fig. 1F–K). Safranin O/Fast green staining of the vertical sections of 9-day chick embryos (Fig. 1M–N) revealed very few Safranin O-positive sites in the ZIKV-infected group compared to those in the control (Fig. 1O), suggesting that abnormal chondrogenesis occurred following ZIKV infection. To observe if osteogenesis was affected by ZIKV infection, we postponed the harvest time of embryos to incubation day 13 (Fig. 2A). Alizarin red staining of the 13-day chick embryos (Fig. 2B–C, B1–C1) showed that the length of premaxilla in ZIKV-infected embryos was much shorter than that in the control embryos (Fig. 2D); meanwhile, the frequency of parietal bone (PA) defect in ZIKV-infected embryos increased significantly (Fig. 2E), and the area of squamosal bone (SQ) in ZIKV-infected embryos reduced dramatically compared to that in the control (Fig. 2F). All of these data imply that ZIKV infection indeed interferes with craniofacial skeleton development.

2.2. ZIKV infection was established and retarded the development of gastrulating chick embryos

The skull develops from the mesenchyme, which is derived from the neural crest and paraxial mesoderm during gastrulation. Therefore, we first determined the general development of HH0 gastrula chick embryos by early chick (EC) culture with or without ZIKV infection (Fig. 3A). With control embryos as the standard, we found that infection with ZIKV at 6.5×10^5 PFU/ml and 6.5×10^4 PFU/ml caused gastrula chick embryo death (Fig. 3B). Using the same strategy, we imaged the developing gastrula embryos at 0, 18, 28, and 40 h (Fig. 3C–J) and observed that the relative lengths (control embryos as reference) of ZIKV-infected embryos at 40 h decreased significantly (Fig. 3K). In fact, developmental retardation occurred at every incubation point of 18, 28, and 40 h, which was determined based on the ratio of developmental velocity of gastrula chick embryos between ZIKV-infected and control embryos (Fig. 3L).

To confirm successful ZIKV infection in early chick embryos, whole mount immunofluorescent staining against ZIKV was implemented in 40-h incubated chick embryos (Fig. 3M–N, M1–N1), and positive expression was clearly observed in the neural tubes of intact embryo (Fig. 3N1) and its corresponding sections (Fig. 3 N2–N3). Moreover, electron microscopy also showed the presence of ZIKV in the neural tube of chick embryo (Fig. 3O), and a group of virus particles with a bright interior could be observed under high magnification (Fig. 3P, indicated by arrows), which indicated that the virus may be replicating (Mlakar et al., 2016b). Simultaneously, both ZIKV PFU (Fig. 3Q) and RNA copy numbers (Fig. 3R) increased in comparison to that in the control. The receptor tyrosine kinase family (TAM) is a family of receptors that assist dengue virus and Zika virus enter the cell(Hamel et al., 2015), so we examined the expression levels of AXL and MERTK in infected chicken embryos (Fig. S1). We observed no significant changes in expression levels of AXL in ZIKV-infected groups (Fig. S1A). However, ZIKV-infected groups expressed higher levels of MERTK when compared to SHAM-infected groups (Fig. S1B). Thus, it was suggested that ZIKV successfully infected early chick embryos and dramatically interfered with the development of gastrula chick embryos.

2.3. ZIKV infection impairs cranial neural crest development in the developing chick embryo

Whole mount immunofluorescent staining for ZIKV and HNK-1, the migratory neural crest cell marker (Erickson et al., 1989; Minarcik and

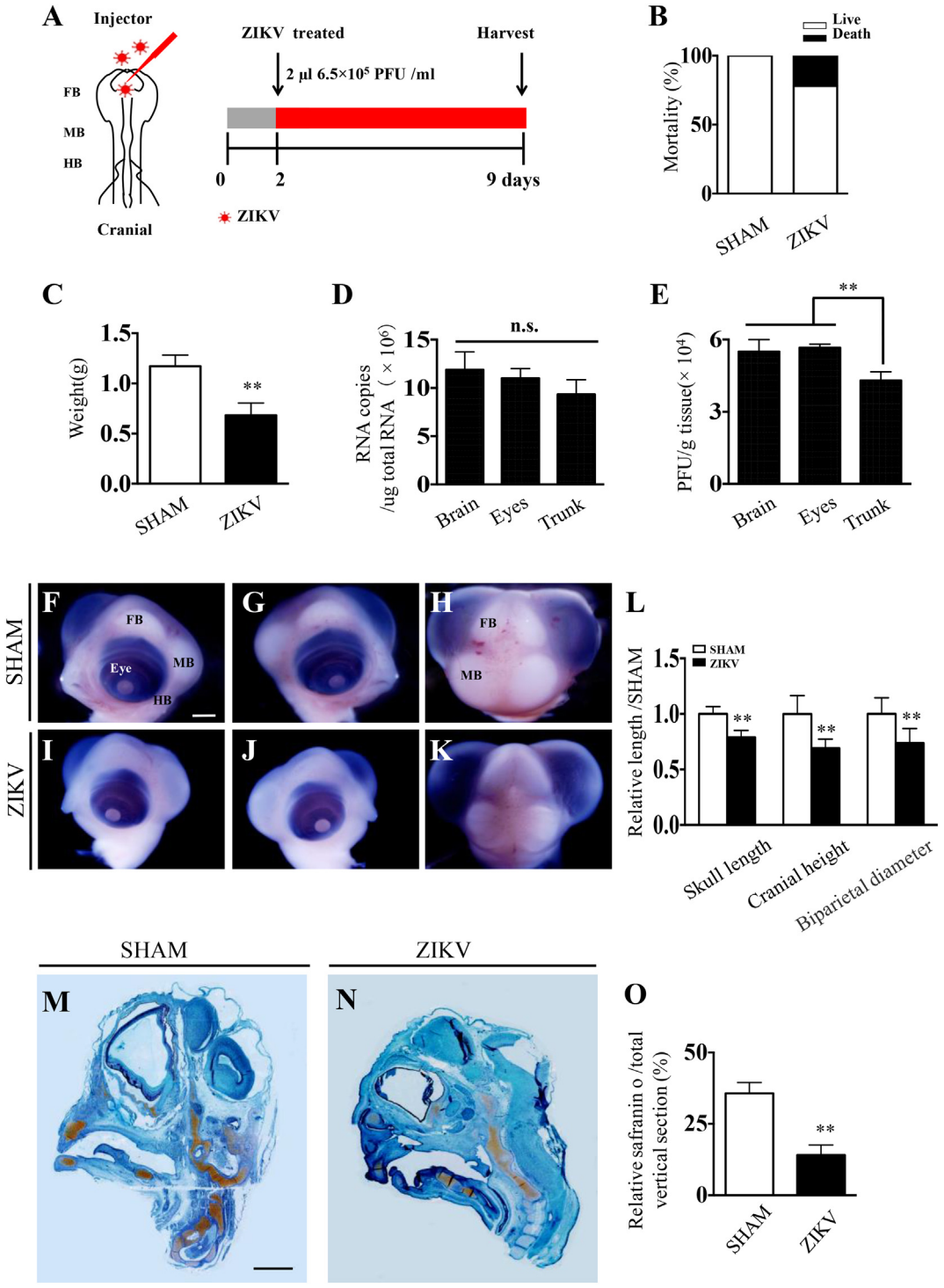

Fig. 1. Head development in chick embryos was morphologically assessed following ZIKV infection.
A: Sketches illustrating that either ZIKV or MEM medium (SHAM) was injected into the cranial neural tubes of 2-day chick embryos, and then the embryos were harvested on day 9. B–C: Bar charts showing embryo mortality (B) and weight (C) comparison between the SHAM and ZIKV-infected groups; Data represent mean ± SD ($n = 6$, ** $P < .01$, Student's *t*-test). D–E: Bar charts showing ZIKV copies (D) and PFU (E) comparison between the SHAM and ZIKV-infected chick embryo tissues, including the brain, eyes, and trunk; Data represent mean ± SD ($n = 3$, **$P < .01$, n.s., not significant, One-way ANOVA with Tukey's multiple comparisons test). F–H: Images are from the right (F), left (G), and upper side (H) of day-9 chick embryo head in the SHAM group. I–K: Images are from the right (I), left (J), and upper side (K) of day-9 chick embryo head in the ZIKV-infected group. L: Bar chart showing comparison of the skull length, cranial height, and biparietal diameter of day-9 chick embryo heads between the SHAM and ZIKV-infected groups; Data represent mean ± SD (n = 6, **$P < .01$, Student's *t*-test). M–N: Representative images of Safranin O/Fast green-stained vertical sections of day-9 chick embryo heads from the SHAM (M) and ZIKV-infected groups (N). O: Bar chart showing the relative area ratio comparisons between the Safranin O-positive area and total vertical section area in the control and ZIKV-infected groups; Data represent mean ± SD ($n = 9$, **$P < .01$, Student's *t*-test). Abbreviation: PFU, plaque forming unit; FB, forebrain; MB, midbrain; HB, hindbrain. Scale bars = 500 μm in F–K and 1000 μm in M–N. (For interpretation of the references to colour in this figure legend, the reader is referred to the web version of this article.)

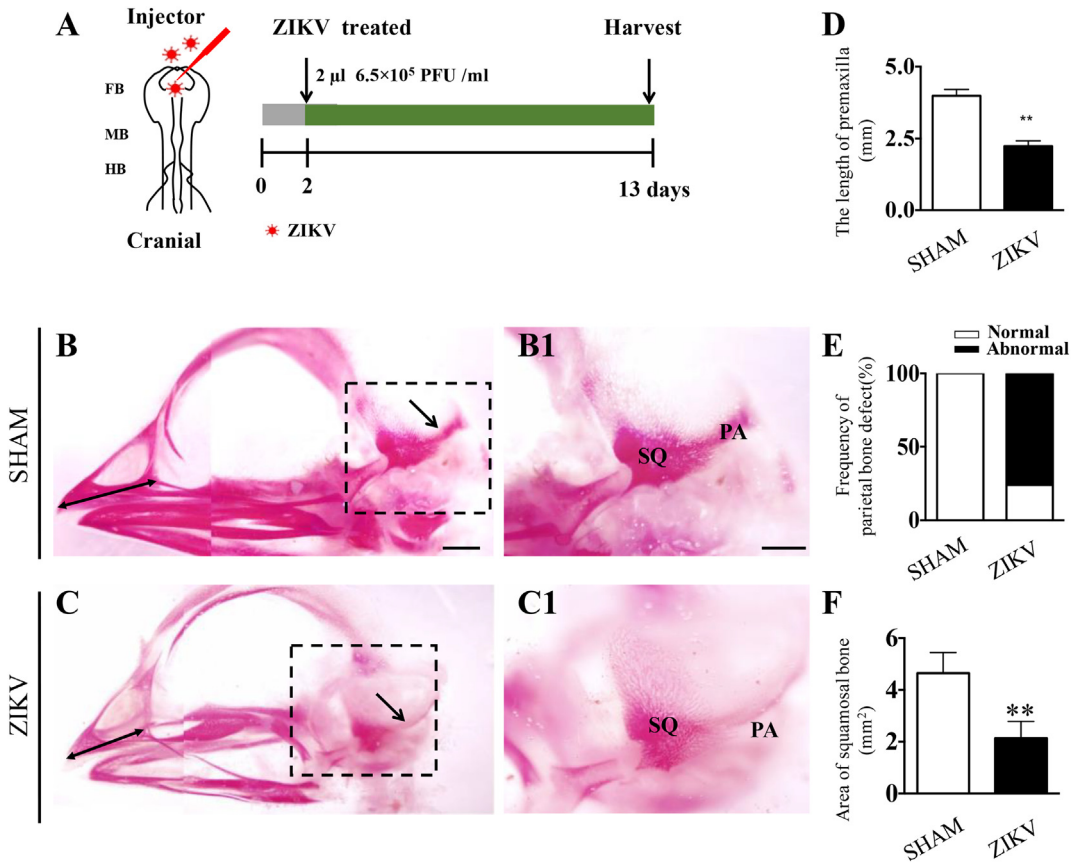

Fig. 2. Alizarin red-stained cranial osteogenesis of chick embryos was assessed following ZIKV infection.
A: Sketches illustrating that either ZIKV or MEM medium (SHAM) was injected into the cranial neural tubes of 2-day chick embryos, and then the embryos were harvested on day 13. B–C: Representative images of alizarin red-stained skulls of 13-day chick embryos from the SHAM (B) and ZIKV-infected (C) groups. B1–C1: High magnification images of the sites indicated by dotted squares in B and C, respectively. D: Bar chart showing comparison of the premaxilla length between the SHAM and ZIKV-infected embryos; Data represent mean ± SD (n = 6, $^{**}P < .01$, Student's *t*-test). E: Bar chart showing the percentages of parietal bone defects in the SHAM and ZIKV-infected embryos. F: Bar chart showing the comparison of the area of squamosal bones between the SHAM and ZIKV-infected embryos; Data represent mean ± SD (n = 6, $^{**}P < .01$, Student's *t*-test). Abbreviation: PA, parietal bone; SQ, squamosal bone FB, forebrain; MB, midbrain; HB, hindbrain. Scale bars = 1000 μm in B–C, B1–C1. (For interpretation of the references to colour in this figure legend, the reader is referred to the web version of this article.)

Golden, 2003), was employed to determine the effect of ZIKV infection on cranial neural crest development (Fig. 4A–F). Double staining showed that the area of ZIKV-positive expression overlapped with HNK-1 at the migratory neural crest (Fig. 4D–F, F1), and HNK-1 expression in ZIKV-infected embryos was less than that in the control (Fig. 4A–C, C1). To further verify the observation, primary culture of neural tube explants from HH10 chick embryos was performed in the presence/absence of ZIKV in the culture medium (Fig. 4G). The extensions of NCC from the incubated ZIKV-infected neural tube explants (Fig. 4H–I) were much shorter than those in the control (Fig. 4J). Double staining of immunofluorescent Zika (green) and HNK-1 (red) demonstrated that majority of the extended cells from the neural tube explants were NCC, *i.e.*, HNK-1 positive (Fig. 4K–P), in which more than a quarter of these were ZIKV-infected cells (Fig. 4Q).

We checked the expressions of AP-2α and Pax7 in ZIKV-infected embryos by immunofluorescent staining (Fig. 5A–D). AP-2α is specifically expressed in the cranial neural crest (Minarcik and Golden, 2003), and Pax7 is expressed in premigratory and migratory NCC (Basch et al., 2006). The results manifested that both AP-2α expression in whole embryos (Fig. 5A–B) and AP-2α -positive cell numbers on the transverse sections (Fig. 5, A1–A2, B1–B2) of ZIKV-infected embryos were significantly repressed compared to those in the controls (Fig. 5E–F), suggesting that ZIKV infection inhibits the production of cranial neural crest. Moreover, we found lower Pax7 expression in ZIKV-infected whole embryos (Fig. 5D) and fewer Pax7-positive cells on transverse sections (Fig. 5D1–D2) than those in the controls (Fig. 5C, C1–C2), implying that ZIKV infection also suppressed the generation of premigratory and migratory NCC. Taken together, both *in vivo* and *in vitro* experimental data indicate that ZIKV infection restricts the production of migratory cranial NCC during early embryo development (Fig. 5I).

2.4. ZIKV-mediated suppression of EMT could be partially responsible for restricting neural crest production

EMT is an indispensable process for neural crest delamination on the dorsal side of the neural tube (Fairchild et al., 2014). Therefore, we determined several crucial factors that regulate EMT during neural crest production. First, whole mount *in situ* hybridization of cadherin 6B (Fairchild et al., 2014), an adhesion molecule, was performed in HH10 chick embryos (Fig. 6A–B), and the results showed that ZIKV infection dramatically increased cadherin 6B expression on the dorsal side of the neural tube (Fig. 6B1–B2, C) compared to that in the control (Fig. 6A1–A2, C). Quantitative PCR data demonstrated that ZIKV infection increased cadherin 6B and N-cadherin expression and down-regulated cadherin 7 expressions at the mRNA level, except for E-cadherin (Fig. 6D). Second, we implemented whole mount *in situ* hybridization for *Slug* and *FoxD3*, which are transcription factors (Fairchild et al., 2014; Naber et al., 2013) that control the above-mentioned EMT adhesion molecules, in HH10 chick embryos (Fig. S2A–D). We observed that both *Slug* and *FoxD3* expressions on the dorsal side of ZIKV-infected embryos (Fig. S2B1–B2, D1–D2) were weaker than those in the controls (Fig. S2A1–A2, C1–C2, S2E–F). ZIKV

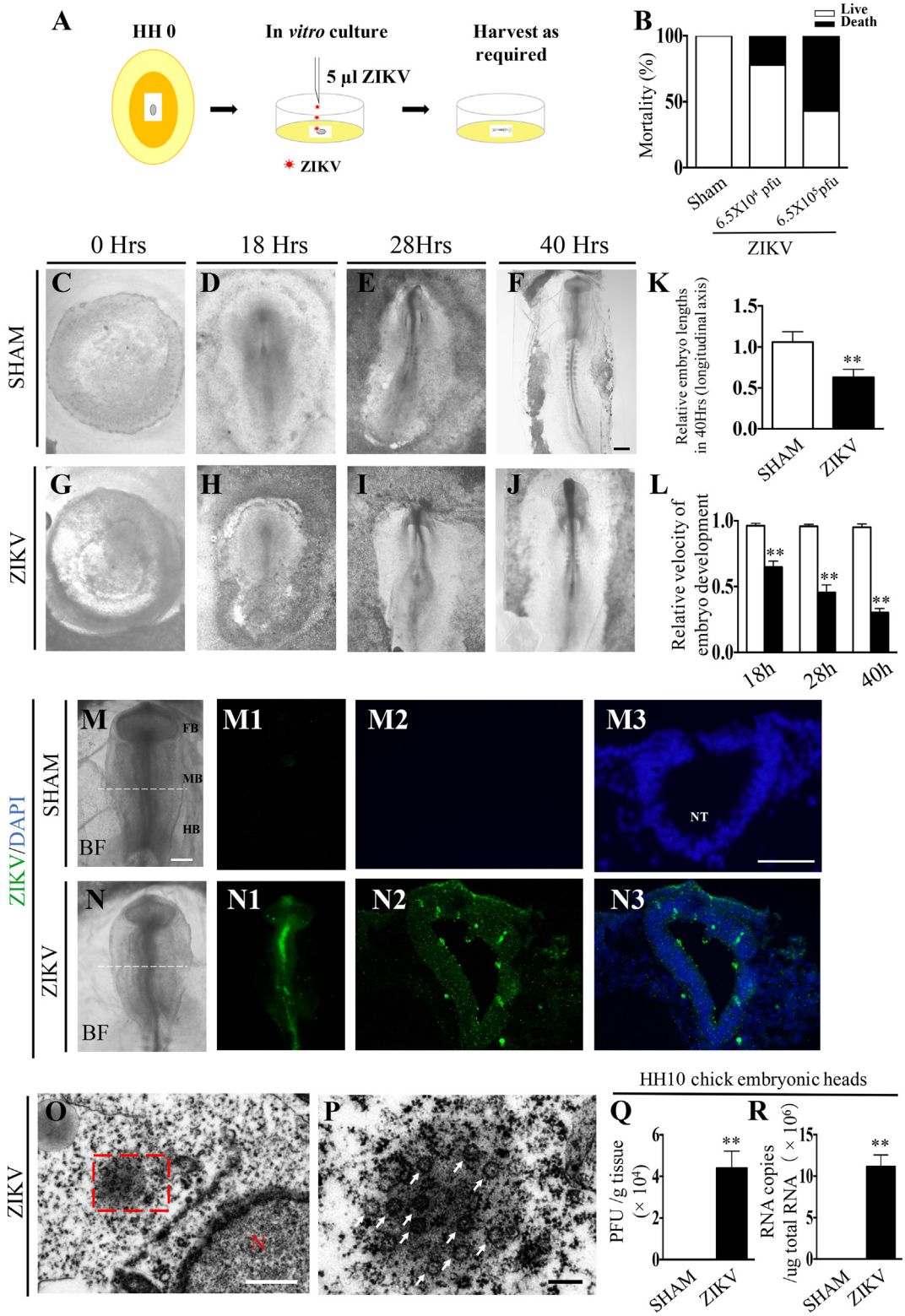

(caption on next page)

suppression of both transcription factors was further verified by quantitative PCR data, in which *Slug* and *FoxD3* expressions in ZIKV-infected neural tubes were much lower than those in the control at the mRNA level (Fig. S2G). Third, we performed *in situ* hybridization of *BMP4* and *Msx1* in HH10 chick embryos (Fig. S3A–D) because BMP4 can upregulate Msx1 expression and then target the EMT process (Sailer et al., 2013). The results showed BMP4 (Fig. S3B1–B2) and Msx1 (Fig. S3D1–D2) expressions were downregulated in ZIKV-infected embryos compared to those in the controls (Fig. S3A1–A2, C1–C2, S3E—F). Similarly, the expressions of both the genes at the mRNA levels were also reduced following ZIKV infection, as revealed by quantitative PCR (Fig. S3G). Taken together, ZIKV infection during early embryo development certainly represses the expressions of EMT-related growth factors, transcription factors, and adhesion molecules, which lead to inhibition

Fig. 3. Assessing development and ZIKA infection in chick gastrula embryos following ZIKV exposure.
A: Sketches illustrating that HH0 chick embryos were incubated with either ZIKV or MEM medium (SHAM) until they reached HH10. B: Bar chart showing death and dysplasia percentages of early chick embryos in the control and ZIKV-infected groups. C–J: Representative bright-field images of chick embryos incubated for 0, 18, 28, and 40 h in the control (C—F) and ZIKV-infected (G–J) groups. K–L: Bar charts showing comparison of the relative length (longitudinal axis) (K) and maturation rate (L) of 40-h incubated embryos between the SHAM and ZIKV-infected groups; Data represent mean ± SD (n = 6, ** $P < .01$, Student's *t*-test). M–N, M1–N1: Bright field (M–N) and anti-ZIKA envelope protein immunofluorescent (M1–N1) images of the cranial portions of 40-h incubated chick embryos from the SHAM (M–M1) and ZIKV-infected (N—N1) groups. M2–N2, M3–N3: Transverse sections of the levels indicated by dotted lines in M and N (M2–N2); M3 and N3 are the merged images of M2–N2 and DAPI staining. O–P: Representative electron microscopic images of the cranial neural tubes of 40-h incubated chick embryos from the ZIKV-infected (O) groups and high magnification images (P) of the sites indicated by red dotted squares in O. Q: Bar chart showing ZIKV PFU in each gram of tissue in the SHAM and ZIKV-infected groups; Data represent mean ± SD ($n = 3$, ** $P < .01$, Student's *t*-test). R: Bar chart showing ZIKV RNA copy numbers in total RNA in the SHAM and ZIKV-infected groups; Data represent mean ± SD (n = 3 technical replicates, **$P < .01$, Student's *t*-test). Abbreviation: FB, forebrain; MB, midbrain; HB, hindbrain; NT, Neural tube; N, nucleus. Scale bars = 1000 μm in C–J; 200 μm in M–N and M1–N1; 50 μm in M2–N2 and M3–N3; 500 nm in O; and 100 nm in P. (For interpretation of the references to colour in this figure legend, the reader is referred to the web version of this article.)

of the EMT process of neural crest delamination on the dorsal side of the neural tubes.

2.5. Inhibition of cranial neural crest production could be due to ZIKV-mediated suppression of cell proliferation and increase in apoptosis

Proliferation and apoptosis certainly could affect the production of NCC during embryo development. Whole mount double immunofluorescent staining of *pHIS3* (red) and *Pax7* (green) (Fig. 7A–B) could reveal whether *pHIS3*-positive cell numbers were altered in Pax7-labeled neural crest following ZIKV infection. It was clearly observed in the transverse sections (Fig. 7A1–A3, B1–B3) that the co-expressed *pHIS3*- and *Pax7*-positive cell numbers in ZIKV-infected embryos were much lower than those in the control (Fig. 7C). To confirm this observation, we implemented *pHIS3* and bromodeoxyuridine (BrdU) immunofluorescent staining on primary culture of NCC *in vitro* with or without ZIKV infection (Fig. 7D–E, G–H) and observed that the percentages of *pHIS3*- (Fig. 7F) and BrdU-positive (Fig. 7I) cell numbers in total DAPI-labeled cell numbers decreased significantly compared to those in the control. This result suggests that ZIKV infection inhibits NCC proliferation during embryo development.

To determine whether apoptosis was affected, we performed cleaved caspase-3 (cl-Casp3; green) and AP-2α (red) double immunofluorescent staining in HH10 chick embryos (Fig. 8A–B) and sectioned the embryos at cranial levels (indicated by dotted lines in Fig. 8A and B). The results distinctly showed high cl-Casp3-positive cranial NCC identified by AP-2α expression in ZIKV-infected embryos (Fig. 8B1–B3) than that in the control (Fig. 8A1–A3, Fig. 10C). Western blot data showed that ZIKV infection increased Pro-casp9, cl-Casp9, Pro-Casp3, and cl-Casp3 expressions compared to those in the control in HH10 chick embryonic tubes, and the ratios of cl-Casp3/Pro-Casp3 and cl-Casp9/Pro-Casp9 were augmented (Fig. 8D). Furthermore, we performed cl-Casp3 immunofluorescent staining on the *in vitro* primary culture of NCC with or without ZIKV infection (Fig. 8E–F), and the results indicated that the percentage of cl-Casp3-positive cells in total DAPI-labeled cell numbers in the ZIKV-infected group was much higher than that in the control (Fig. 8G). Therefore, these results indicated that ZIKV infection leads to the increase in apoptosis of developing cranial NCC.

As a cell survival mechanism, autophagy could be activated by infection, but excessive activation could lead to cell death (Wang et al., 2015; Pei et al., 2015). We observed a number of autophagosomes (indicated by arrows) in ZIKV-infected chick embryonic neural tubes by electron microscopy (Fig. 9A–C). Western blot data showed that ZIKV infection increased *Atg7*, *Beclin-1*, and *LC3BII/LC3BI* expressions and decreased *mTOR* and *P62* expressions in HH10 chick embryos (Fig. 9D). Moreover, double immunofluorescent staining of ZIKV and LC3B on *in vitro* primary culture of NCC confirmed that LC3B expressions were much higher in ZIKV-infected embryos than those in the control (Fig. 9E–J), suggesting that ZIKV infection may lead to excessive autophagy, which, in turn, could enhance apoptosis in the neural crest.

3. Discussions

ZIKV is an emerging mosquito-borne flavivirus, and it was first isolated from a rhesus macaque in Uganda > 70 years ago (Dick et al., 1952). Maternal ZIKV intrauterine infection during pregnancy is associated with the increased incidence of fetal defects, especially abnormal nervous system in infants or fetuses (Mlakar et al., 2016a; Oliveira Melo et al., 2016). Microcephaly and other serious brain abnormalities were considered to be due to dysplasia of the brain induced by ZIKV infection (Tsai, 2006). The evidence includes identification of ZIKV in fetal brain tissues and fetal brain anomaly by electron microscopy and autopsy (Mlakar et al., 2016a). At present, the research on the pathogenesis of ZIKV-induced brain mal-development was mainly focused on neural precursor cells, neurospheres and brain-like organoids. These studies indicated that ZIKV crossed the placenta and caused microcephaly by targeting cortical neural progenitor cells, inducing cell death and impairing neurodevelopment (Cugola et al., 2016). However, there is another type of cells, neural crest cells, playing a crucial role in the process of human brain development. Our results confirmed that ZIKV could infect cranial neural crest cells (Fig. 4).

Intramembranous ossification is the main form of osteogenesis in the skull, and cranial NCC are principal components of progenitor cells that differentiate into mesenchymal cells, in which ossification occurs later (Santagati and Rijli, 2003). Because most of the craniofacial structures, including most of the bones and cartilages, which shape the developing fetal brain, are derived from cranial NCC, we studied the effect of ZIKV infection on the development of cranial neural crest using early chick embryos. We chose chick embryo as the experimental model in this study for the following reasons: ZIKV can cross the placental barrier to infect the developing embryos; therefore, the developing chick embryo would reasonably mimic mammalian embryo development. Moreover, its characteristics of rapid development and accessibility for experimental manipulation render virus infection in developing chick embryos easy at any developmental stage (Vergara and Canto-Soler, 2012).

Using quantitative PCR and electron microscopy (Figs. 1D–E and 3O–R), we showed that the early chick embryos were successfully infected by ZIKV in this study. ZIKV-infected chick embryo development was generally slower than that of control gastrula embryos, which is consistent with the previous report about gross intrauterine fetal growth retardation following ZIKV infection (Mlakar et al., 2016a). It has been suggested that abnormal development of the brain size and other systems is observed, although the phenotype of microcephaly is predominant following ZIKV infection in the embryo. This observation generally fits well with the wide distribution of ZIKV infection observed in the early chick embryos, which slightly contradicts a previous report on strong neurotropism exhibited by ZIKV because it was not found in any other organs except for the brain (Mlakar et al., 2016a). The most important finding of our study was that ZIKV infection suppressed cranial osteogenesis and reduced the brain size of chick embryos (Figs. 1F–O and 2). Subsequently, we demonstrated that ZIKV was detected in the migratory neural crest (Fig. 4C1 and F1) and ZIKV-

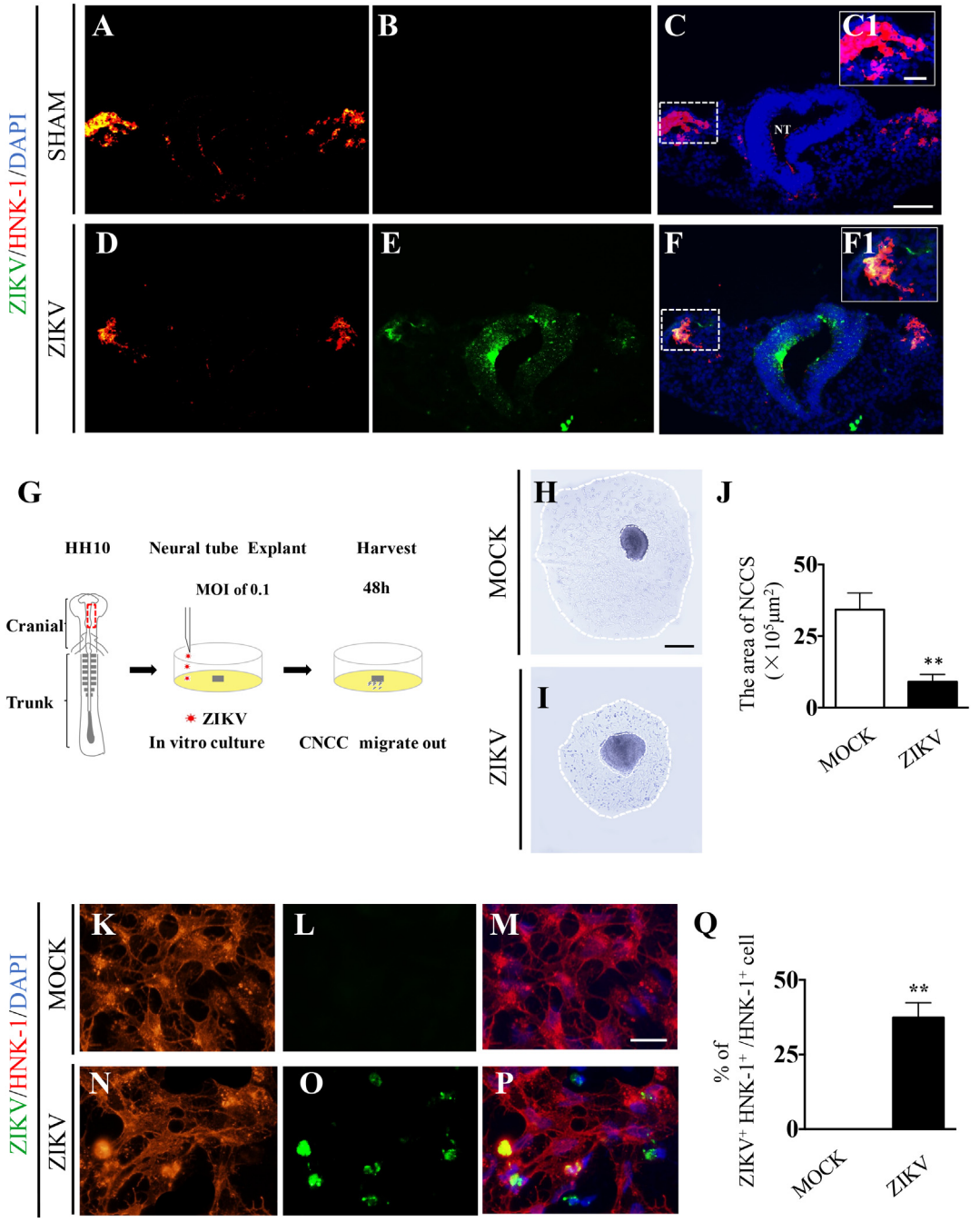

Fig. 4. Assessing HNK1-positive neural crest production in chick embryos following ZIKV infection.
A–F: Representative transverse sections of HNK1 (A, D) and anti-ZIKA envelope protein (B, E) immunofluorescent-stained HH10 chick embryos and merged images of A–B or D–E and DAPI staining (C–F) from the SHAM (A–C) and ZIKV-infected (D–F) groups. C1, F1: High magnification images of the sites indicated by dotted squares in C and F, respectively. G: Sketches illustrating that the neural tube explants from HH10 chick embryos were excised and then incubated *in vitro* with either ZIKV or DMEM medium (MOCK) for 48 h. H–I: Representative bright-field images of 48-h incubated neural tube explants from the MOCK (H) and ZIKV-infected groups (I). J: Bar chart showing the comparison of the area of cranial NCC extended from the neural tube explants in the MOCK and ZIKV-infected groups; Data represent mean ± SD ($n = 9$, ** $P < .01$, Student's *t*-test). K–P: Representative images of HNK1 (K, N) and anti-ZIKA envelope protein (L, O) immunofluorescent stained NCC extended from the neural tube explants after 48-h incubation, and merged image of K–L or N–O and DAPI staining (M, P) from the MOCK (K–M) and ZIKV-infected (N–P) groups (MOI of 0.1 for 48 h). Q: Bar chart showing the percentages of ZIKV- and HNK1-positive cells in total HNK1-positive cells in the MOCK and ZIKV-infected groups; Data represent mean ± SD ($n = 9$, ** $P < .01$, Student's *t*-test). Abbreviation: NT, Neural tube. Scale bars = 50 μm in A–F; 25 μm in C1 and F1; 400 μm in H and I; and 25 μm in K–P.

inhibited cranial osteogenesis was observed at the stage of neural crest development, since we observed the inhibition of HNK-1-labeled migratory NCC *in vivo* and *in vitro* (Fig. 4) induced by ZIKV infection in the neural tube, where neural crest delamination occurs (Fig. 3M–R). Using the specific cranial neural crest marker AP-2α, we verified ZIKV infection-mediated reduction in neural crest development in the cranial neural crest. Furthermore, because Pax7 is expressed in the premigratory and migratory neural crest, the decrease in Pax7-positive cells induced by ZIKV infection (Fig. 5) suggests that ZIKV infection surely affects cranial neural crest migration from the neural tube, thereby confining cranial osteogenesis.

EMT is an indispensable process for stratification of neural crest

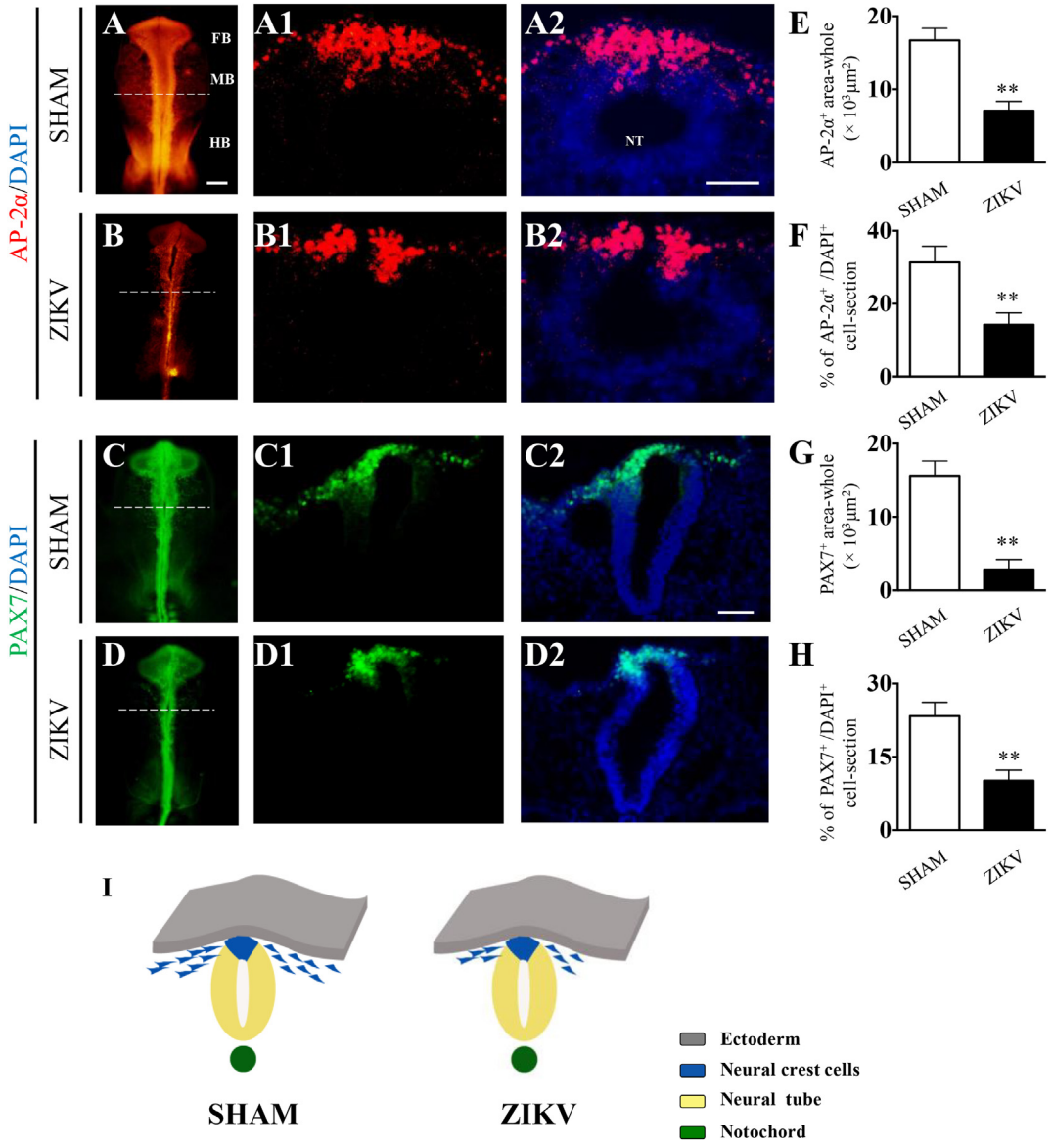

Fig. 5. *Assessing AP-2α- and Pax7-positive neural crest production in chick embryos following ZIKV infection.*
A–B: Representative images of AP-2α immunofluorescent staining at the cranial portion of HH10 chick embryos from the SHAM (A) and ZIKV-infected (B) groups. A1–B1, A2–B2: A1 and B1 are the transverse sections of the levels indicated by dotted lines in A and B, respectively. A2 and B2 are the merged images of A1–B1 and DAPI staining. E–F: Bar charts showing the ratios of AP-2α-positive cells in whole mount chick embryos (E), and the percentages of AP-2α-positive cells in total transverse sections (F) in the SHAM and ZIKV-infected groups; Data represent mean ± SD ($n = 9$, $^{**}P < .01$, Student's *t*-test). C–D: Representative images of Pax7 immunofluorescent staining at the cranial portion of HH10 chick embryos from the SHAM (C) and ZIKV-infected (D) groups. C1–D1, C2–D2: C1 and D1 are the transverse sections of the levels indicated by dotted lines in C and D, respectively. C2 and D2 are the merged images of C1–D1 and DAPI staining. G–H: Bar charts showing the ratios of Pax7-positive cells in whole mount chick embryos (G), and the percentages of Pax7-positive cells in total transverse sections (H) in the SHAM and ZIKV-infected groups; Data represent mean ± SD (n = 9, $^{**}P < .01$, Student's *t*-test). I: Sketches illustrating the alteration of delaminated NCC on the dorsal side of neural tubes following ZIKV infection. Abbreviation: FB, forebrain; MB, midbrain; HB, hindbrain; NT, Neural tube. Scale bars = 200 μm in A–D and 50 μm in A1–B2 and C1–D2.

cells, so we carefully studied the expressions of vital adhesion molecules (cadherin 6B, N-cadherin, cadherin 7 and E-cadherin), transcription factors (*Slug* and *FoxD3*), and BMP4/Msx1 signaling because they coordinately control the EMT of cranial NCC in the neural tube (Fig. 6, S2-S3). Inhibition of *Msx1* expression may partially contribute to the interference with the generation and differentiation of cranial NCCs. Bmp4, a downstream target of Msx1, plays an important role in the initiation and differentiation of NCC as well during alveolar bone formation (Zhang et al., 2003). Cad6B (epithelial cadherin-6B) is an adhesion molecule that responds to EMT in chick cranial neural crest (Maharajan et al., 2016), indicating that Cad6B downregulation is absolutely required for NCC migration from the neural tube (Rothan et al., 2018). In this study, we found that ZIKV-infection upregulated adhesion molecules and downregulated transcription factors and BMP/Msx1, which partially blocked EMT. Given the aforementioned phenotypes of the premigratory and migratory stage of neural crest development, we concluded that ZIKV targets every step of early neural crest development, including delamination, EMT, and migration. With respect to the cellular mechanism of ZIKV infection-induced aberrant neural crest development, we discovered that cranial neural crest cell proliferation was dramatically inhibited (Fig. 7) and apoptosis was promoted (Fig. 8) by ZIKV infection in an chick embryo model, which has also been observed previously in an *in vitro* model of embryonic stem cells (Bayless et al., 2016). Consistent with our findings, a large number of reports in

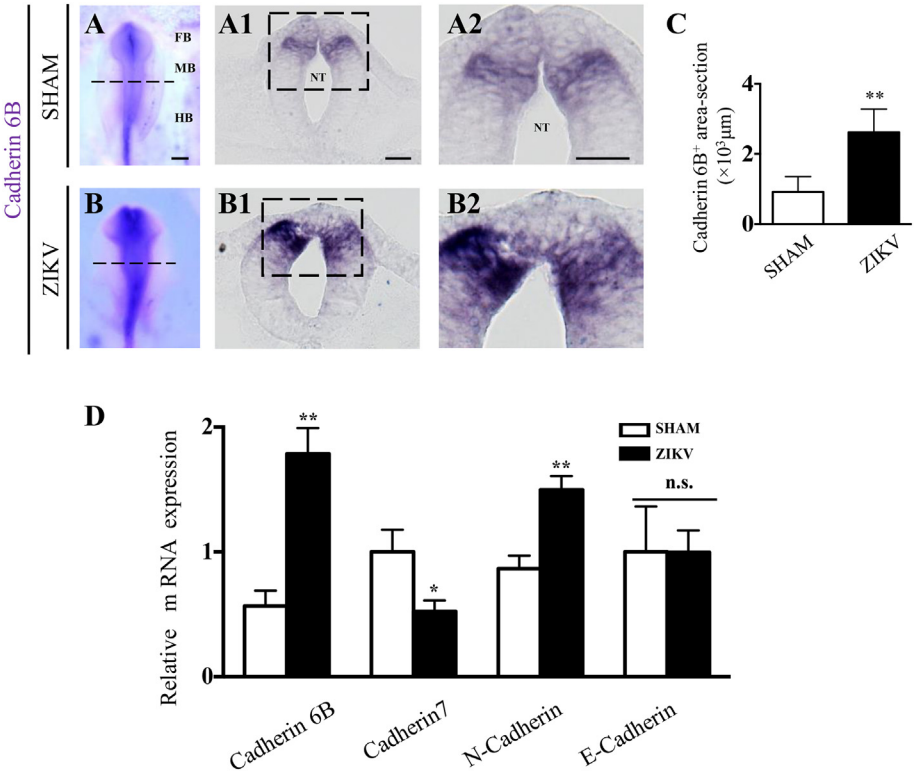

Fig. 6. *In situ* hybridization and quantitative PCR to determine the expressions of adhesion molecules in chick embryos following ZIKV infection.
A–B: Whole mount cadherin 6B *in situ* hybridization was performed in HH10 chick embryos. Representative images of the cranial portions of embryos from the SHAM (A) and ZIKV-infected (B) groups. A1–B1: Transverse sections of the levels indicated by dotted lines in A and B, respectively. A2–B2: High magnification images of the sites indicated by dotted squares in A1 and B1, respectively. C: Bar chart showing the comparison of cadherin 6B-positive areas on the transverse sections (A2–B2) between the SHAM and ZIKV-infected groups; Data represent mean ± SD (n = 9, ** $P < .01$, Student's t-test). D: Quantitative PCR data showing the relative mRNA expressions of cadherin 6B, cadherin 7, N-cadherin, and E-cadherin in the neural tubes of the SHAM and ZIKV-infected groups; Data represent mean ± SD ($n = 3$, *$P < .05$, ** $P < .01$, n.s., not significant, Student's t-test). Abbreviation: FB, forebrain; MB, midbrain; HB, hindbrain; NT, Neural tube. Scale bars = 200 μm in A–B and 25 μm in A1–B1 and A2–B2.

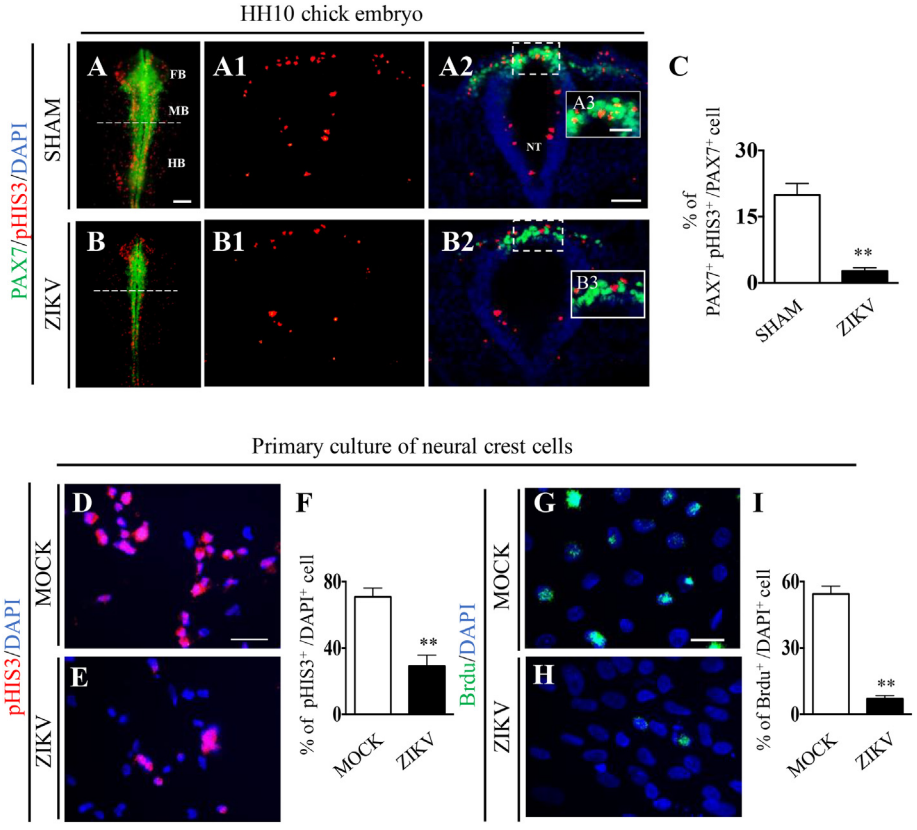

Fig. 7. Assessing the effect of ZIKV infection on cell proliferation for cranial neural crest development in chick embryos.
A–B: Double immunofluorescent staining of *Pax7* and *pHIS3* was performed. Representative images of the cranial portions of HH10 chick embryos from the SHAM (A) and ZIKV-infected (B) groups. A1–B1, A2–B2: Transverse sections of the levels indicated by dotted lines in A and B, respectively. A1–B1 are pHIS3 staining only, whereas A2–B2 are the merged images of *Pax7* (green), *pHIS3* (red), and DAPI staining (blue). A3–B3: High magnification images of the sites indicated by dotted squares in A2 and B2, respectively. C: Bar charts showing the percentages of *Pax7* and *pHIS3* co-positive cells in total Pax7-positive cells in the transverse sections (A2–B2) of the SHAM and ZIKV-infected groups; Data represent mean ± SD (n = 9, ** $P < .01$, Student's t-test). D–E: pHIS3 immunofluorescent staining and DAPI staining on the primary culture of NCC from the MOCK (D) and ZIKV-infected (E) groups (MOI of 0.1 for 48 h). F: Bar chart showing the percentages of *pHIS3*-positive cells in total DAPI-stained primary cultured NCC (D–E) in the MOCK and ZIKV-infected groups; Data represent mean ± SD (n = 9, **$P < .01$, Student's t-test). G–H: BrdU immunofluorescent staining and DAPI staining on the primary culture of NCC from the MOCK (G) and ZIKV-infected (H) groups (MOI of 0.1 for 48 h). I: Bar chart showing the percentages of BrdU-positive cells in total DAPI-stained primary cultured NCC (G–H) in the MOCK and ZIKV-infected groups; Data represent mean ± SD (n = 9, **$P < .01$, Student's t-test). Abbreviation: FB, forebrain; MB, midbrain; HB, hindbrain; NT, Neural tube. Scale bars = 200 μm in A–B; 50 μm in A1–B1 and A2–B2; and 25 μm in A3–B3, D–E, and G–H. (For interpretation of the references to colour in this figure legend, the reader is referred to the web version of this article.)

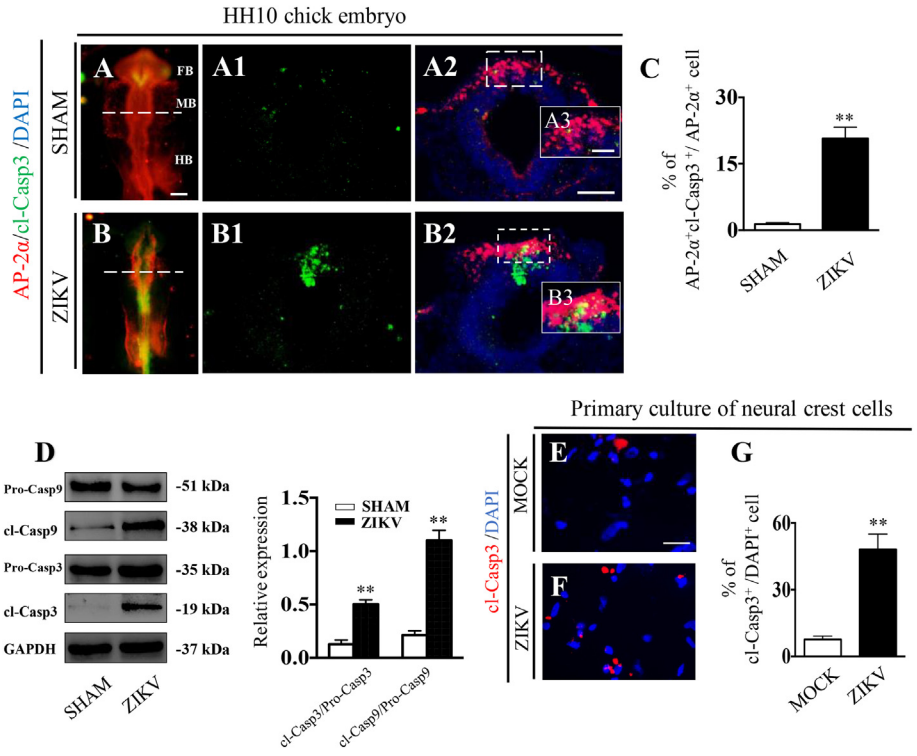

Fig. 8. Assessing the effect of ZIKV infection on apoptosis of cranial neural crest cell production in chick embryos.
A–B: Double immunofluorescent staining of Ap-2α and cleaved caspase-3 (cl-Casp3) was performed. Representative images of the cranial portions of HH10 chick embryos of the SHAM (A) and ZIKV-infected (B) groups. A1–B1, A2–B2: Transverse sections of the levels indicated by dotted lines in A and B, respectively. A1–B1 are cl-Casp3 staining only, whereas A2–B2 are the merged images of cl-Casp3 (green), AP-2α (red), and DAPI staining (blue). A3–B3: High magnification images of the sites indicated by dotted squares in A2 and B2, respectively. C: Bar chart showing the percentages of AP-2α and cl-Casp3 co-positive cells out of total Pax7-positive cells in the transverse sections (A2–B2) of the SHAM and ZIKV-infected groups; Data represent mean ± SD (n = 9, ** $P < .01$, Student's t-test). D: Western blot showing pro-caspase-9, cl-Casp9, pro-caspase-3, and cl-Casp3 expressions at the protein level in the neural tubes of the SHAM and ZIKV-infected groups; Bar chart showing the comparison of caspase-9 and caspase-3 relative expressions (cl-Casp/Pro-casp) in the neural tubes of the control and ZIKV-infected groups; Data represent mean ± SD (n = 3, **$P < .01$, Student's t-test). E–F: cl-Casp3 immunofluorescent staining and DAPI staining on the primary culture of NCC of the MOCK (E) and ZIKV-infected (F) groups (MOI of 0.1 for 48 h). G: Bar chart showing the percentages of cl-Casp3-positive cells in total DAPI-stained primary cultured NCC (E–F) in the MOCK and ZIKV-infected groups; Data represent mean ± SD (n = 9, ** $P < .01$, Student's t-test). Abbreviation: cl-Casp3, cleaved caspase-3; cl-Casp9, cleaved caspase-9. Abbreviation: FB, forebrain; MB, midbrain; HB, hindbrain; NT, Neural tube. Scale bars = 200 μm in A–B; 50 μm in A1–B1 and A2–B2; and 25 μm in A3–B3 and E–F. (For interpretation of the references to colour in this figure legend, the reader is referred to the web version of this article.)

cortical neurons and their precursor cells suggested that viral infection-mediated cell death was a key molecular mechanism for pathogenesis of ZIKV in humans. Studies in human neural stem cells induced from pluripotent stem cells had shown that ZIKV infection could cause developmental inhibition and cell death of cortical neurons, neurospheres, and brain-like systems or models through TLR3 activation (Tang et al., 2016; Dang et al., 2016; Garcez et al., 2016). In the fetal mouse model of ZIKV infection, the 'vacuolar nuclei' appearance could be observed *in situ* in cortical neurons, indicating a massive cell death (Cugola et al., 2016). Of course, increased apoptosis during neural crest development could also be one of the reasons for aberrant development of the neural crest following ZIKV infection. Furthermore, ZIKV can activate autophagy, an intracellular process wherein broken cytoplasmic constituents are recruited and fuse with lysosomes for protein degradation (Blazquez et al., 2014). However, excessive autophagy could lead to cell death. We established that ZIKV infection greatly enhanced the levels of autophagy in the developing neural crest using electron microscopy, western blot, and immunofluorescent staining (Fig. 9).

In summary, our data, particularly from *in vivo* experiments, first show that ZIKV infection during gestation could interfere with the normal development of cranial neural crest, including delamination, EMT, cell survival, migration, and differentiation processes during early embryogenesis. Moreover, aberrant NCC would lead to the dysplasia of cranial osteogenesis because cranial NCCs are the progenitor cells of bone formation in the skull. Our findings were also supported by a recent study in neural crest cell models derived from human embryonic stem cells (Oh et al., 2017). Consistent with our findings, their results also showed that ZIKV directly infected neural crest cells and induced cell death. A large number of previous studies had confirmed that cortical neuron damage was a possible cause of ZIKV infection-mediated brain malformation. ZIKV infection-mediated neural crest cells would aggravate this damage. Bayless et al. (Bayless et al., 2016) used an *in vitro* model of co-culture of neural crest cells and embryonic stem cells to detect dysregulation of neurogenesis caused by harmful cytokines secreted by NCC after ZIKV infection. We believe that the mechanisms of fetal brain development abnormalities (especially microcephaly) caused by Zika virus infection are multifactorial, and our findings partially complement the underlying mechanisms between them (Fig. 10). However, whether the differentiation process of NCC into mesenchymal cells is impaired and osteogenesis *per se* is impaired are still obscure. Therefore, more studies on the precise molecular mechanism are required in the future.

4. Materials and methods

4.1. Viral culture and amplification

ZIKV (KU955589.1) used for the experiment was isolated from a Chinese clinical case and was presented by Professor Zhao Wei of Southern Medical University. *Aedes albopictus* clone C6/36(C6/36) cells used to amplify the virus were purchased from ATCC (American Type Culture Collection; USA). C6/36 cells were cultured in MEM medium (Gibco, USA), containing 10% fetal bovine serum (Gibco, USA), 1% non-essential amino acid (Gibco, USA), 1% sodium pyruvate (Gibco, USA), 1% penicillin/streptomycin (Gibco, USA), and 0.05% amphotericin B (Gibco, USA), and were incubated without CO_2 at 28 °C. After C6/36 cells reached approximately 70% monolayer confluency, 50 μl of the virus stock was inoculated, adsorbed for 2 h, and gently rocked every 10 min to allow uniform adsorption of the virus. At the end of adsorption, 5 ml of the medium supplemented with 5% FBS, 1% non-essential amino acids, and 1% sodium pyruvate was added. The cultures were then incubated under the same conditions. On the 5th day after infection, the supernatant (centrifugal 10 min at 4000 *g*, 4 °C) was collected, titrated, aliquoted, and stored at −80 °C. All experiments involving ZIKV were performed under biosafety level 2 (BSL-2) class at Jinan University, China. Experiments were performed under the

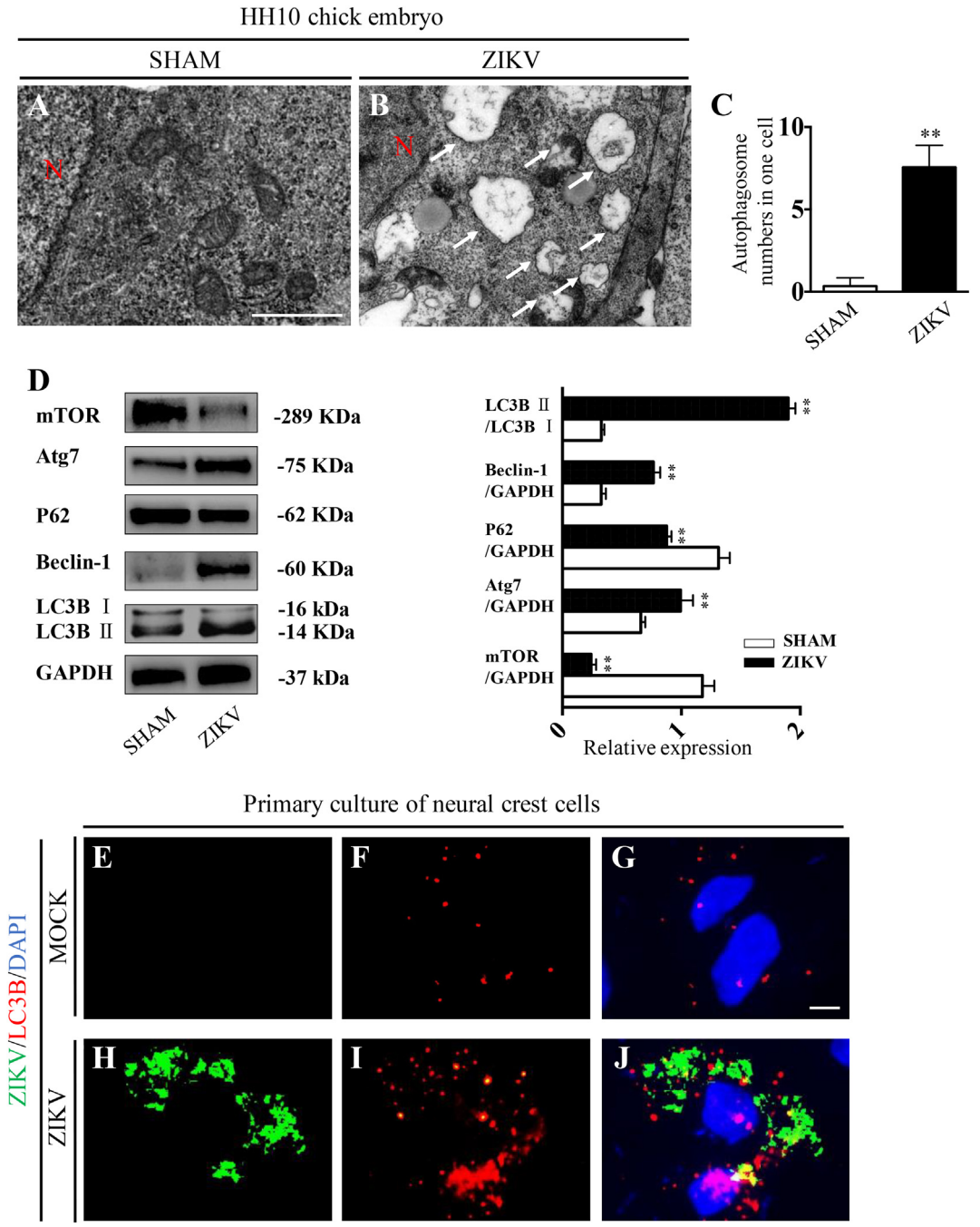

Fig. 9. Assessing the effect of ZIKV infection on autophagy of cranial neural crest cell production in chick embryos.
A–B: Representative electron microscopic images of the cranial neural tubes of the SHAM (A) and ZIKV-infected (B) groups. C: Bar chart showing autophagosome numbers in each cell by electron microscopy (A–B) in the SHAM and ZIKV-infected groups; Data represent mean ± SD (n = 9, $^{**}P < .01$, Student's t-test). D: Western blot showing mTOR, Atg7, P62, Beclin-1, and LC3B I/LC3 BII expressions at protein level in the neural tubes of the SHAM and ZIKV-infected groups; bar chart showing the comparison of LC3B, Beclin-1, P62, and Atg7 relative expressions in the neural tubes of the SHAM and ZIKV-infected groups; Data represent mean ± SD (n = 3, $^{**}P < .01$, Student's t-test). E–J: Representative images of anti-ZIKA envelope protein (E, H), LC3B (F, I), immunofluorescent stained NCC extending from the neural tube explants after 48-h incubation, and merged images of E–F or H–I and DAPI staining (G, J) of the SHAM (E–G) and ZIKV-infected (H–J) groups (MOI of 0.1 for 48 h). Abbreviation: N, nucleus. The white arrow indicates the autophagosome. Scale bars = 1 μm in A–B and 5 μm in E–J.

supervision and assessment of the Laboratory Animal Ethics Committee of Jinan University.

4.2. ZIKV plaque assay

Baby Hamster Syrian Kidney(BHK)-21(ATCC; USA) monolayers were infected with 10-fold serial dilutions of virus-infected tissue homogenate supernatants and incubated at 37 °C for 4–6 h to initiate binding to the cells. A mixture of 2% carboxymethyl cellulose (CMC) and the culture broth was used. Then, the cells were covered and infected for four days. For plaque counts, cells were fixed with 4% formaldehyde for 1 h and then stained with 0.1% crystal violet (in 20% ethanol) for 15 min. The virus titer was calculated as plaque forming unit (PFU) per ml.

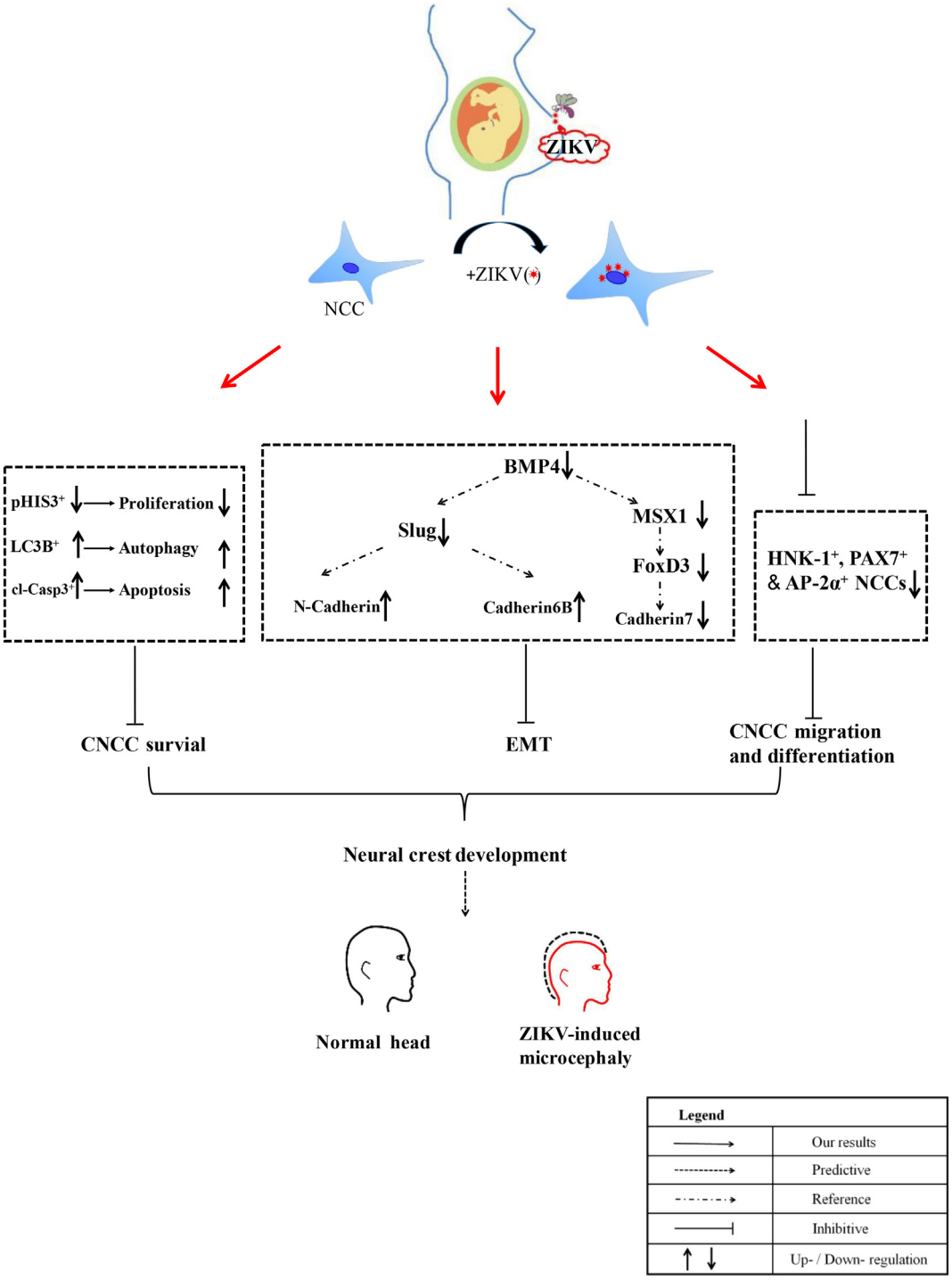

Fig. 10. Model depicting why cranial osteogenesis is responsible for ZIKA infection-induced brain malformations.
ZIKV infection during gestation negatively influences development of the cranial neural crest, in which abnormal cranial osteogenesis (microcephaly) occurs.

4.3. Chick embryos and ZIKV manipulation

Fertilized leghorn eggs were acquired from the Avian Farm of South China Agriculture University (Guangzhou, China). Two approaches were employed to perform ZIKV infection in this study. For ZIKV infection at the early embryonic stage, Hamburger–Hamilton (HH) (Hamburger and Hamilton, 1951) 0 stage chick embryos from the fertilized eggs were incubated with either MEM medium (control) or ZIKV at 6.5×10^4 PFU/ml in the early chick (EC) (Chapman et al., 2001) culture medium in a humidified incubator (Yiheng Instruments, Shanghai, China) at 38 °C and 70% humidity until the chick embryos developed to HH10 stage. For ZIKV infection at the later embryonic stage, pre-incubated 2-day fertilized eggs were windowed; either MEM medium (control) or ZIKV 6.5×10^5 PFU/ml were injected into the cranial neural tubes of chick embryo in the windowed eggs. The windows in the eggs were sealed and further incubated until day 9 or 13 for embryo harvesting, and surviving embryos were harvested for various assessments.

4.4. Safranin O/Fast green staining

Paraffin sections were dewaxed in succession with xylene and

absolute ethanol and were then rinsed with tap water. The slices were immersed in a solid green dye bath for 5–10 min, and excess dye was washed with water until the cartilage was colorless. The slides were slightly soaked in differentiation solution and washed with tap water. The slices were then immersed in alcoholic Safranin for 15–30 s and rapidly dehydrated by three cylinders of anhydrous ethanol. The sections were then made transparent with clear xylene for 5 min, and neutral gels were used to seal the slides. Sections were imaged and analyzed using a microscope (Olympus IX51epi, Japan).

4.5. Alizarin red staining of whole embryos

The craniofacial skeleton was visualized in 13-day-old chick embryos by staining with alizarin red dye (Solarbio, Beijing, China).Briefly, the embryos were fixed in 95% ethanol for three days, and the skin and viscera were then carefully removed before post-fixation for an additional day. The embryos were then pretreated in 0.5% KOH for 48 h before staining with alizarin red dye suspended in 0.5% KOH for three days. Finally, the embryos were cleared in graded series of glycerol. The craniofacial skeleton was photographed using a stereomicroscope (Olympus MVX10, Japan).

4.6. Immunofluorescent staining

Chick embryos were harvested after incubation and fixed in 4% paraformaldehyde (PFA; Newprobe Bioscience Technology Co. Ltd., Beijing, China) overnight at 4 °C. Whole-mount embryo immunofluorescent staining or primary explant was performed using the corresponding antibodies (Supplementary Table S1). Briefly, the fixed chick embryos were incubated with the primary antibodies at 4 °C overnight on a shaker. After extensive rinsing in PBST (phosphate buffered saline with 0.1% Tween-20), the embryos were treated with the corresponding Alexa Fluor® 555 or 488 labeled secondary antibody (Supplementary Table S2) at 4 °C overnight on a shaker. For double immunofluorescent staining, the antibodies were incubated one after the other. All the embryos were later counterstained with DAPI (1:1000, Invitrogen) at room temperature for 1 h. Subsequently, the stained embryos were sectioned at 10 μm using a cryostat (Leica CM1900).

4.7. Western blot

HH10 chick embryos were collected and lysed with CytoBuster™ Protein Extraction Reagent (#71009, Novagen , USA). Total protein concentrations were assessed using a BCA quantification kit (BCA01, DingGuo BioTECH, China). Samples containing identical amounts of protein were fractionated by SDS-PAGE and then transferred to PVDF membranes (Bio-Rad, USA). Membranes were blocked with 5% Difco™ skim milk (BD) and subsequently incubated with primary and secondary antibodies, and the bands of interest protein were visualized using the ECL kit (#34079, Thermo Scientific, USA) and GeneGnome5 (SYNGENE). The gray scale of bands was analyzed using Quantity One software (Bio-Rad, USA). The corresponding primary and secondary antibodies are shown in Supplementary Tables S1 and S2. All primary antibodies were diluted to 1000-fold in 5% skim milk, and secondary antibodies were diluted to 2000-fold in 5% skim milk.

4.8. In situ hybridization

Whole-mount *in situ* hybridization of chick embryos was performed according to the standard *in situ* hybridization protocol (Fernandez-Garcia et al., 2009). Digoxigenin-labeled probes were synthesized to detect *Msx1*, *Slug*, *FoxD3*, *BMP4*, and *Cad6B* mRNAs. A digoxigenin-labeled probe was synthesized for *Slug* (Nieto et al., 1994). Other primers used to generate the *in situ* hybridization probes are shown in Supplementary Table S3. Whole-mount stained embryos were photographed, and the frozen sections at thickness of 20 μm were prepared from these embryos for histological analysis.

4.9. RNA isolation and qPCR analysis

Total RNA was isolated from HH10 chick embryos using a TRIzol kit (Invitrogen, USA) according to the manufacturer's instructions. The ZIKV-specific primer/probe set was synthesized by Sigma Life Science, and 5-carboxyfluorescein (5-FAM) was used as the reporter group for the probe (Supplementary Table S4). Real-time fluorescence quantitative reactions were performed using the One Step PrimeScriptTM RT-PCR Kit (TaKaRa, Japan). Amplification was performed in a Bio-Rad CFX 96 real-time PCR system (BioRad, USA) at 42 °C for 5 min, 95 °C for 10 s, 40 cycles of 95 °C for 5 s, and 60 °C for 34 s. The CFX manager software (BioRad, USA) was used to analyze the real-time data. The viral RNA copy number was quantified, and the cycle threshold (Ct value) of real-time PCR for each sample was compared with the ZIKV plasmid standard curve.

For detection of other genes, first-strand cDNA synthesis and SYBR® Green qPCR assay were performed using the PrimeScript™ RT reagent kit (TaKaRa, Japan). All specific primers used are mentioned in Supplementary Table S4. Reverse transcription and amplification reactions were performed in Bio-Rad S1000™ (Bio-Rad, USA) and Bio-Rad CFX 96 (Bio-Rad, USA), respectively. The housekeeping gene *GAPDH* was run in parallel to confirm that equal amounts of RNA were used in each reaction. The ratio between the intensity of the fluorescently stained bands corresponding to the genes and *GAPDH* was calculated to quantify the level of the transcripts for the genes. The RT-PCR result was representative of three independent experiments.

4.10. Primary NCC cultures

NCC were isolated from the cranial neural tubes of chick embryos according to previously described methods (Etchevers, 2011). Briefly, fertilized chick eggs were incubated until the 7–9 somite stage (HH9). The neural tube was then dissected from the head region of the embryo and explanted into 3.5-mm dishes, containing DMEM and 10% FBS, for 6 h at 37 °C and 5% CO_2 to allow the explants to adhere. The explants were incubated until a few NCC were observed migrating out of the neural tubes, and then 1 ml of the culture medium containing DMEM (control) or ZIKV (10 μl of 6.5×10^5 PFU/2 ml in DMEM supplemented with 5% FBS) was introduced into the cultures. The treated explants were allowed to develop for 48 h, and then the areas containing the migrant NCC were measured and analyzed using Image-Pro Plus 7.0 (Media Cybernetics, USA). After incubation, NCC cultures were washed with pre-warmed PBS and fixed in PFA. The fixed cells were washed three times with 1× PBS and blocked with blocking solution (10% goat serum in 0.1% Triton-X 100 in PBS) for 90 min. The corresponding antibody (Supplementary Table S1) was diluted with blocking buffer and incubated overnight at 4 °C. The cells were washed with 1× PBS, and the corresponding secondary antibody (Supplementary Table S2) was added at a dilution of 1:1000 in blocking buffer and incubated for 1 h at room temperature. Cells were washed with 1× PBS, and nuclei were stained with 4′,6-diamidino-2-phenylindole (DAPI; 1:1000; Invitrogen, USA), and cells were observed under a fluorescence microscope (Olympus IX51epi, Japan) or a Rapid Laser Scanning Confocal Microscopy (Leica, Germany).

4.11. Microscopy

Light microscopy: Following immunofluorescent staining, whole mount embryos and regions of interest were photographed using a stereo fluorescence microscope (Olympus MVX10, Japan) and processed using Olympus software package Image-Pro Plus 7.0. The embryos were then sectioned at 20 μm using a cryostat microtome (Leica CM1900), photographed using an Olympus IX51epi-fluorescent

microscope, and analyzed using the CW4000 FISH Olympus software.

Transmission electron microscopy: Control and ZIKV-infected HH10 chick embryos were fixed with 2.5% glutaraldehyde in 0.1 M PBS for 2 h, and the neural tubes were then dissected. The samples were sent to the TEM Laboratory of Jinan University. Embedding, ultrathin sectioning, and staining were performed by professional technicians and examined using a Tecnai G2 Spirit Twin (FEI, USA).

4.12. Data analysis

All data analyses and graphics were performed using the Graphpad Prism 5 software (Graphpad Software, CA, USA). The results were presented as the mean value ($\bar{x} \pm$ SD). All data were analyzed using *t*-test or ANOVA to establish the difference between the experimental and control groups, $^{*}p < .05$, $^{**}p < .01$ and n.s. for not significant. $p < .05$ was considered statistically significant.

Supplementary data to this article can be found online at https://doi.org/10.1016/j.meegid.2019.01.023.

Declaration of interests

The authors declare no competing financial interests.

Acknowledgements

This study was supported by National Natural Science Foundation of China (81473454 and 31771331), Science and Technology Planning Project of Guangdong Province (2017A050506029). This study also received assistance from Natural Science Foundation of Guangdong, China (2015A030313331), and from the National science and technology major projects of China (2018ZX10715004-002).

References

Basch, M.L., Bronner-Fraser, M., Garcia-Castro, M.I., 2006. Specification of the neural crest occurs during gastrulation and requires Pax7. Nature 441 (7090), 218–222.
Bayless, N.L., Greenberg, R.S., Swigut, T., Wysocka, J., Blish, C.A., 2016. Zika virus infection induces cranial neural crest cells to produce cytokines at levels detrimental for neurogenesis. Cell Host Microbe 20 (4), 423–428.
Besnard, M., Lastere, S., Teissier, A., Cao-Lormeau, V., Musso, D., 2014. Evidence of perinatal transmission of Zika virus, French Polynesia, December 2013 and February 2014. Euro Surveill. 19 (13).
Blazquez, A.B., Escribano-Romero, E., Merino-Ramos, T., Saiz, J.C., Martin-Acebes, M.A., 2014. Stress responses in flavivirus-infected cells: activation of unfolded protein response and autophagy. Front. Microbiol. 5, 266.
Bronner, M.E., 2015. Evolution: on the crest of becoming vertebrate. Nature 527 (7578), 311–312.
Calvet, G., Aguiar, R.S., Melo, A.S.O., Sampaio, S.A., de Filippis, I., Fabri, A., et al., 2016. Detection and sequencing of Zika virus from amniotic fluid of fetuses with microcephaly in Brazil: a case study. Lancet Infect. Dis. 16 (6), 653–660.
Chapman, S.C., Collignon, J., Schoenwolf, G.C., Lumsden, A., 2001. Improved method for chick whole-embryo culture using a filter paper carrier. Dev. Dyn. 220 (3), 284–289.
Cofre, F., 2016. Zika virus intrauterine infection causes fetal brain abnormality and microcephaly: tip of the iceberg? Rev. Chil. Infectol. 33 (1), 96.
Cordero, D.R., Brugmann, S., Chu, Y., Bajpai, R., Jame, M., Helms, J.A., 2011. Cranial neural crest cells on the move: their roles in craniofacial development. Am. J. Med. Genet. A 155A (2), 270–279.
Cugola, F.R., Fernandes, I.R., Russo, F.B., Freitas, B.C., Dias, J.L., Guimaraes, K.P., et al., 2016. The Brazilian Zika virus strain causes birth defects in experimental models. Nature 534 (7606), 267–271.
Dang, J., Tiwari, S.K., Lichinchi, G., Qin, Y., Patil, V.S., Eroshkin, A.M., et al., 2016. Zika virus depletes neural progenitors in human cerebral organoids through activation of the innate immune receptor TLR3. Cell Stem Cell 19 (2), 258–265.
Datar, S.P., Bhonde, R.R., 2011. Modeling chick to assess diabetes pathogenesis and treatment. Rev. Diabet. Stud. 8 (2), 245–253.
Dick, G.W., 1952. Zika virus. II. Pathogenicity and physical properties. Trans. R. Soc. Trop. Med. Hyg. 46 (5), 521–534.
Dick, G.W., Kitchen, S.F., Haddow, A.J., 1952. Zika virus. I. Isolations and serological specificity. Trans. R. Soc. Trop. Med. Hyg. 46 (5), 509–520.
Erickson, C.A., Loring, J.F., Lester, S.M., 1989. Migratory pathways of HNK-1-immunoreactive neural crest cells in the rat embryo. Dev. Biol. 134 (1), 112–118.
Etchevers, H., 2011. Primary culture of chick, mouse or human neural crest cells. Nat. Protoc. 6 (10), 1568–1577.
Fairchild, C.L., Conway, J.P., Schiffmacher, A.T., Taneyhill, L.A., Gammill, L.S., 2014. FoxD3 regulates cranial neural crest EMT via downregulation of tetraspanin18 independent of its functions during neural crest formation. Mech. Dev. 132, 1–12.
Fernandez-Garcia, M.D., Mazzon, M., Jacobs, M., Amara, A., 2009. Pathogenesis of flavivirus infections: using and abusing the host cell. Cell Host Microbe 5 (4), 318–328.
Garcez, P.P., Loiola, E.C., Madeiro da Costa, R., Higa, L.M., Trindade, P., Delvecchio, R., et al., 2016. Zika virus impairs growth in human neurospheres and brain organoids. Science 352 (6287), 816–818.
Hall, B.K., 2008. The neural crest and neural crest cells: discovery and significance for theories of embryonic organization. J. Biosci. 33 (5), 781–793.
Hamburger, V., Hamilton, H.L., 1951. A series of normal stages in the development of the chick embryo. J. Morphol. 88 (1), 49–92.
Hamel, R., Dejarnac, O., Wichit, S., Ekchariyawat, P., Neyret, A., Luplertlop, N., et al., 2015. Biology of Zika Virus Infection in Human Skin Cells. J. Virol. 89 (17), 8880–8896.
Maharajan, M.K., Ranjan, A., Chu, J.F., Foo, W.L., Chai, Z.X., Lau, E.Y., et al., 2016. Zika virus infection: current concerns and perspectives. Clin. Rev. Allergy Immunol. 51 (3), 383–394.
Minarcik, J.C., Golden, J.A., 2003. AP-2 and HNK-1 define distinct populations of cranial neural crest cells. Orthod. Craniofacial Res. 6 (4), 210–219.
Mlakar, J., Korva, M., Tul, N., Popovic, M., Poljsak-Prijatelj, M., Mraz, J., et al., 2016a. Zika virus associated with microcephaly. N. Engl. J. Med. 374 (10), 951–958.
Mlakar, J., Korva, M., Tul, N., Popovic, M., Poljsak-Prijatelj, M., Mraz, J., et al., 2016b. Zika virus associated with microcephaly. N. Engl. J. Med. 374 (10), 951–958.
Naber, H.P., Drabsch, Y., Snaar-Jagalska, B.E., ten Dijke, P., van Laar, T., 2013. Snail and Slug, key regulators of TGF-beta-induced EMT, are sufficient for the induction of single-cell invasion. Biochem. Biophys. Res. Commun. 435 (1), 58–63.
Nieto, M.A., Sargent, M.G., Wilkinson, D.G., Cooke, J., 1994. Control of cell behavior during vertebrate development by Slug, a zinc finger gene. Science 264 (5160), 835–839.
Oh, Y., Zhang, F., Wang, Y., Lee, E.M., Choi, I.Y., Lim, H., et al., 2017. Zika virus directly infects peripheral neurons and induces cell death. Nat. Neurosci. 20 (9), 1209–1212.
Oliveira Melo, A.S., Malinger, G., Ximenes, R., Szejnfeld, P.O., Alves Sampaio, S., Bispo de Filippis, A.M., 2016. Zika virus intrauterine infection causes fetal brain abnormality and microcephaly: tip of the iceberg? Ultrasound Obstet. Gynecol. 47 (1), 6–7.
Pei, F., Lin, H., Liu, H., Li, L., Zhang, L., Chen, Z., 2015. Dual role of autophagy in lipopolysaccharide-induced preodontoblastic cells. J. Dent. Res. 94 (1), 175–182.
Penchaszadeh, V.B., Velasquez, D., Arrivillaga, R., 1982. The nasopalpebral lipoma-coloboma syndrome: a new autosomal dominant dysplasia-malformation syndrome with congenital nasopalpebral lipomas, eyelid colobomas, telecanthus, and maxillary hypoplasia. Am. J. Med. Genet. 11 (4), 397–410.
Petersen, E.E., Polen, K.N., Meaney-Delman, D., Ellington, S.R., Oduyebo, T., Cohn, A., et al., 2016. Update: interim guidance for health care providers caring for women of reproductive age with possible Zika Virus Exposure—United States, 2016. MMWR Morb. Mortal. Wkly Rep. 65 (12), 315–322.
Rodriguez-Morales, A.J., 2015. Zika: the new arbovirus threat for Latin America. J. Infect. Dev. Countries 9 (6), 684–685.
Rothan, H.A., Bidokhti, M.R.M., Byrareddy, S.N., May 2018. Current concerns and perspectives on Zika virus co-infection with arboviruses and HIV. J. Autoimmun. 89, 11–20.
Sailer, M.H., Gerber, A., Tostado, C., Hutter, G., Cordier, D., Mariani, L., et al., 2013. Non-invasive neural stem cells become invasive in vitro by combined FGF2 and BMP4 signaling. J. Cell Sci. 126 (Pt 16), 3533–3540.
Santagati, F., Rijli, F.M., 2003. Cranial neural crest and the building of the vertebrate head. Nat. Rev. 4 (10), 806–818.
Schneider, R.A., 1999. Neural crest can form cartilages normally derived from mesoderm during development of the avian head skeleton. Dev. Biol. 208 (2), 441–455.
Scott-Drechsel, D.E., Rugonyi, S., Marks, D.L., Thornburg, K.L., Hinds, M.T., 2013. Hyperglycemia slows embryonic growth and suppresses cell cycle via cyclin D1 and p21. Diabetes 62 (1), 234–242.
Simoes-Costa, M., Bronner, M.E., 2015. Establishing neural crest identity: a gene regulatory recipe. Development (Cambridge, England) 142 (2), 242–257.
Tang, H., Hammack, C., Ogden, S.C., Wen, Z., Qian, X., Li, Y., et al., 2016. Zika Virus Infects Human Cortical Neural Progenitors and Attenuates their Growth. Cell Stem Cell 18 (5), 587–590.
Tappe, D., Perez-Giron, J.V., Zammarchi, L., Rissland, J., Ferreira, D.F., Jaenisch, T., et al., 2016. Cytokine kinetics of Zika virus-infected patients from acute to reconvalescent phase. Med. Microbiol. Immunol. 205 (3), 269–273.
Tetro, J.A., 2016. Zika and microcephaly: causation, correlation, or coincidence? Microbes Infect. 18 (3), 167–168.
Triunfol, M., 2016. A new mosquito-borne threat to pregnant women in Brazil. Lancet Infect. Dis. 16 (2), 156–157.
Tsai, T.F., 2006. Congenital arboviral infections: something new, something old. Pediatrics 117 (3), 936–939.
Vergara, M.N., Canto-Soler, M.V., 2012. Rediscovering the chick embryo as a model to study retinal development. Neural Dev. 7, 22.
Vesnaver, T.V., Tul, N., Mehrabi, S., Parissone, F., Strafela, P., Mlakar, J., et al., 2017. Zika virus associated microcephaly/micrencephaly-fetal brain imaging in comparison with neuropathology. BJOG 124 (3), 521–525.
Wang, X.Y., Li, S., Wang, G., Ma, Z.L., Chuai, M., Cao, L., et al., 2015. High glucose environment inhibits cranial neural crest survival by activating excessive autophagy in the chick embryo. Sci. Rep. 5, 18321.
Zhang, Z., Song, Y., Zhang, X., Tang, J., Chen, J., Chen, Y., 2003. Msx1/Bmp4 genetic pathway regulates mammalian alveolar bone formation via induction of Dlx5 and Cbfa1. Mech. Dev. 120 (12), 1469–1479.